

1 **Rigorous 3-D modeling of the ground electric field in**
2 **Fennoscandia during the Halloween geomagnetic storm**

3 **Elena Marshalko¹, Mikhail Kruglyakov², Alexey Kuvshinov³, and Ari**
4 **Viljanen¹**

5 ¹Finnish Meteorological Institute, Helsinki, Finland

6 ²University of Otago, Dunedin, New Zealand

7 ³Institute of Geophysics, ETH Zürich, Zürich, Switzerland

8 **Key Points:**

- 9 • 3-D GEF modeling in Fennoscandia is performed for the Halloween geomagnetic
10 storm using three different approaches to approximate the source
11 • The highest correlation between GEF-based and observed GIC is achieved by us-
12 ing the “conductivity-based” approach
13 • Critical dependence of the GEF on the earth conductivity is demonstrated

Corresponding author: Elena Marshalko, elena.marshalko@fmi.fi

Abstract

In this study, we perform rigorous three-dimensional (3-D) ground electric field (GEF) modeling in Fennoscandia for three days of the Halloween geomagnetic storm (29-31 October 2003) using magnetic field data from the IMAGE magnetometer network and a 3-D conductivity model of the region. To explore the influence of the inducing source model on the 3-D GEF simulations, we considered three different approaches to approximate the source. Within the first two approaches, the source varies laterally, whereas in the third method, the GEF is calculated by implementing the time-domain realization of the magnetotelluric intersite impedance method. We then compare GEF-based geomagnetically induced current (GIC) with observations at the Mäntsälä natural gas pipeline recording point. We conclude that a high correlation between modeled and recorded GIC is observed for all considered approaches. The highest correlation is achieved when performing a 3-D GEF simulation using a “conductivity-based” laterally nonuniform inducing source. Our results also highlight the strong dependence of the GEF on the earth’s conductivity distribution.

Plain Language Summary

Geomagnetically induced currents (GIC) flow in technological conductor systems during geomagnetic variations. Their simulation is of practical interest, since in the worst case, GIC can even cause power grid blackouts. The critical parameter in GIC modeling is the ground electric field (GEF) at the earth’s surface. GEF is rarely measured directly, so it needs to be simulated based on other geophysical data. The modeling input consists of earth electrical conductivity models and ground magnetic field data recorded by magnetometers. Based on the fundamental laws of electrodynamics, it is possible to calculate the GEF at any point on the earth’s surface. From the known GEF, GIC can be determined as well. This study discusses several GEF modeling techniques. Results of modeling during the Halloween geomagnetic storm in October 2003 are validated against GIC observations in Fennoscandia. The study also demonstrates that a conductivity model is a critical factor in estimating GIC since the magnitude of the GEF can decrease or increase many times over short distances due to lateral conductivity variations.

1 Introduction

The so-called Halloween geomagnetic storm on 29-31 October 2003 is one of the largest geomagnetic storms in the history of observations, which also appeared to be very well recorded due to the increase in the scientific instrumentation at that time (Pulkkinen et al., 2005). The Halloween storm consisted of a series of events. The first phase of the storm, which was caused by an arrival of an interplanetary coronal mass ejection (ICME), started with a sudden southward turning of the interplanetary magnetic field (IMF) at about 05:40 UT, 29 October 2003. The second phase started at about 14:00 UT, 29 October 2003, when the internal field of the ejecta itself caused another southward IMF event. Soon after the passage of the first ICME, another hit the magnetosphere. Strong southward turning of the IMF was observed at L1 Lagrange point at about 18:20 UT, 30 October 2003, and was soon followed by a minimum Disturbance storm time index (Dst) of about -400 nT with very strong substorm-related activity in the ionosphere. During this third phase of the storm, the Malmö region in southern Sweden experienced a large-scale blackout caused by the geomagnetic activity. A thorough analysis and the timeline of the Halloween geomagnetic storm can be found in Pulkkinen et al. (2005).

According to Faraday’s law, the fluctuation of the geomagnetic field during space weather events leads to the generation of the ground electric field (GEF), which in turn drives currents in the earth and ground-based technological systems, such as power grids and pipelines (Viljanen & Pirjola, 1994). These geomagnetically induced currents (GIC) can have negative impact on the operation of technological networks. Although widespread

irreversible damage to power systems is unlikely (Pulkkinen et al., 2017), extreme GIC can cause blackouts over extended areas, as it happened in the Malmö region on 30 October 2003.

The primary aim of the current study is to perform rigorous three-dimensional (3-D) GEF modeling in Fennoscandia during the Halloween geomagnetic storm using available observed geomagnetic field data (Tanskanen, 2009) and a 3-D conductivity model of the region (Korja et al., 2002). As it was mentioned by Pulkkinen et al. (2017), from the engineering point of view, the spatiotemporal characteristics of the horizontal GEF provide the ideal description of a geomagnetic disturbance. Simulated GEF data of a very intense event can serve as a reference point for evaluating possible risks to ground-based technological systems in Fennoscandia from space weather, as GIC can be calculated based on the GEF data in the region, the geometry of a technological network and system design parameters (Lehtinen & Pirjola, 1985; Pirjola et al., 2022).

Worth attention, the GEF and GIC in the Fennoscandian region, and also elsewhere in Europe, have been previously modeled in several projects as described by, e.g., Viljanen et al. (2014) and Myllys et al. (2014). Wei et al. (2013) followed a similar idea to model the GEF in North America. A key difference to the present work is that usually to calculate the GEF, researchers employ the plane wave method; moreover, in most studies, only 1-D ground conductivity models have been utilized. Although different 1-D models were used for different locations, the 1-D approach cannot take properly into account effects in the GEF arising from lateral gradients in 3-D conductivity distributions (Ivannikova et al., 2018; Rosenqvist & Hall, 2019; Marshalko et al., 2020; Kelbert, 2020).

To explore the influence of the inducing source model on the 3-D GEF simulations, we considered three different approaches to approximate the source. Noteworthy, all methods exploit the same IMAGE magnetic field data to simulate the GEF, rely on the same 3-D conductivity model of the region, and use the same forward problem engine. Within the first two approaches, the source varies laterally and is factorized by spatial modes (SM) and respective expansion coefficients. In both approaches the SM are the same and are obtained following the two-step numerical scheme introduced by Kruglyakov, Kuvshinov, and Marshalko (2022). The difference between methods lies in the calculation of the expansion coefficients. The details on these two approaches (and the reasoning to invoke the second approach) are presented in Section 2.1. Within the third approach (discussed in the same section), the GEF is calculated by implementing the time-domain realization of the magnetotelluric (MT) intersite impedance method.

Further, in Section 3 we present the results of the source recovery using the first two approaches and the results of the GEF modeling obtained using three considered methods. Besides, we explore in this section how well the observed time series of GIC at Mäntsälä natural gas pipeline recording point (Viljanen et al., 2006) during the Halloween storm are reproduced through a linear combination of the simulated horizontal GEF components at this point. We note once again that the Halloween event is chosen because it is a representative example of a big geomagnetic storm causing the largest value of GIC in the Finnish natural gas pipeline (Dimmock et al., 2019).

A summary of the results and discussion on the possible ways forward are presented in Section 4.

2 Methodology

In this section, we present and discuss three approaches which we invoke to calculate the time-domain GEF. First two methods rely on laterally varying inducing source models, the third one – on the plane-wave excitation. EM modeling is performed for three days (72 hours) of the Halloween geomagnetic storm (29-31 October 2003).

113 2.1 GEF modeling with laterally varying source

114 2.1.1 Governing equations in the frequency domain

115 We start with the discussion of the problem in the frequency domain. Maxwell's
 116 equations govern EM field variations and, in the frequency domain, these equations read
 117 as

$$\frac{1}{\mu_0} \nabla \times \mathbf{B} = \sigma \mathbf{E} + \mathbf{j}^{\text{ext}}, \quad (1)$$

$$\nabla \times \mathbf{E} = i\omega \mathbf{B}, \quad (2)$$

where μ_0 is the magnetic permeability of free space; ω is angular frequency; $\mathbf{j}^{\text{ext}}(\mathbf{r}, \omega)$ is the extraneous (inducing) electric current density; $\mathbf{B}(\mathbf{r}, \omega; \sigma)$ and $\mathbf{E}(\mathbf{r}, \omega; \sigma)$ are magnetic and electric fields, respectively; $\sigma(\mathbf{r})$ is the spatial distribution of electrical conductivity; $\mathbf{r} = (x, y, z)$ is a position vector, in our case in the Cartesian geometry. Note that we neglected displacement currents and adopted the following Fourier convention:

$$f(t) = \frac{1}{2\pi} \int_{-\infty}^{\infty} f(\omega) e^{-i\omega t} d\omega. \quad (3)$$

118 In problem setups, when a laterally nonuniform source is considered, we assume that the
 119 current density, $\mathbf{j}^{\text{ext}}(\mathbf{r}, \omega)$, can be represented as a linear combination of SM $\mathbf{j}_i(\mathbf{r})$:

$$\mathbf{j}^{\text{ext}}(\mathbf{r}, \omega) = \sum_{i=1}^L c_i(\omega) \mathbf{j}_i(\mathbf{r}). \quad (4)$$

120 The form of SM $\mathbf{j}_i(\mathbf{r})$ (and their number, L) varies with application. For example, $\mathbf{j}^{\text{ext}}(\mathbf{r}, \omega)$
 121 is parameterized via spherical harmonics (SH) in Püthe and Kuvshinov (2013b); Honko-
 122 nen et al. (2018); Guzavina et al. (2019); Grayver et al. (2021); Kruglyakov, Kuvshinov,
 123 and Nair (2022), current loops in Sun and Egbert (2012), eigenmodes from the Princi-
 124 pal Component Analysis (PCA) of the physics-based models in Egbert et al. (2021) and
 125 Zenhausern et al. (2021), and eigenmodes from the PCA of the data-based models in Kruglyakov,
 126 Kuvshinov, and Marshalko (2022). In this paper, we will use parameterization adopted
 127 in the latter paper.

128 By virtue of the linearity of Maxwell's equations with respect to the $\mathbf{j}^{\text{ext}}(\mathbf{r}, \omega)$ term,
 129 we can expand electric and magnetic fields as linear combinations of individual fields \mathbf{E}_i
 130 and \mathbf{B}_i ,

$$\mathbf{E}(\mathbf{r}, \omega; \sigma) = \sum_{i=1}^L c_i(\omega) \mathbf{E}_i(\mathbf{r}, \omega; \sigma), \quad (5)$$

$$\mathbf{B}(\mathbf{r}, \omega; \sigma) = \sum_{i=1}^L c_i(\omega) \mathbf{B}_i(\mathbf{r}, \omega; \sigma), \quad (6)$$

131 where $\mathbf{E}_i(\mathbf{r}, \omega; \sigma)$ and $\mathbf{B}_i(\mathbf{r}, \omega; \sigma)$ fields are “electric” and “magnetic” solutions of the fol-
 132 lowing Maxwell's equations:

$$\frac{1}{\mu_0} \nabla \times \mathbf{B}_i = \sigma \mathbf{E}_i + \mathbf{j}_i, \quad (7)$$

$$\nabla \times \mathbf{E}_i = i\omega \mathbf{B}_i. \quad (8)$$

133 2.1.2 Governing equations in the time domain

The transformation of Equations (5) and (6) into the time domain leads to the representation of the electric and magnetic fields as

$$\mathbf{E}(\mathbf{r}, t; \sigma) = \sum_{i=1}^L \int_0^{\infty} c_i(t - \tau) \mathbf{E}_i(\mathbf{r}, \tau; \sigma) d\tau, \quad (9)$$

$$\mathbf{B}(\mathbf{r}, t; \sigma) = \sum_{i=1}^L \int_0^{\infty} c_i(t - \tau) \mathbf{B}_i(\mathbf{r}, \tau; \sigma) d\tau. \quad (10)$$

The reader is referred to Appendix A in Kruglyakov, Kuvshinov, and Marshalko (2022) for more details on the convolution integrals in the above equations. We note that we use the same notation for the fields in the time and frequency domains. Equations (9) and (10) show how the fields can be calculated provided $c_i(t)$ and conductivity model σ are given. To make formulas ready for implementation, one needs to estimate the upper limits of integrals in the above equations, or, in other words, to evaluate time intervals, T_E and T_B , above which $\mathbf{E}_i(\mathbf{r}, \tau; \sigma)$ and $\mathbf{B}_i(\mathbf{r}, \tau; \sigma)$ become negligibly small. The latter will allow us to approximate Equations (9) and (10) as

$$\mathbf{E}(\mathbf{r}, t; \sigma) \approx \sum_{i=1}^L \int_0^{T_E} c_i(t - \tau) \mathbf{E}_i(\mathbf{r}, \tau; \sigma) d\tau, \quad (11)$$

$$\mathbf{B}(\mathbf{r}, t; \sigma) \approx \sum_{i=1}^L \int_0^{T_B} c_i(t - \tau) \mathbf{B}_i(\mathbf{r}, \tau; \sigma) d\tau. \quad (12)$$

The details of numerical calculation of the integrals in the above equations are presented in Kruglyakov, Kuvshinov, and Marshalko (2022) and Kruglyakov, Kuvshinov, and Nair (2022). Assuming that time series $c_i(t)$ are given with the sampling interval Δt , one calculates $\mathbf{E}(\mathbf{r}, t_k; \sigma)$ and $\mathbf{B}(\mathbf{r}, t_k; \sigma)$ at $t_k = k\Delta t$ as

$$\mathbf{E}(\mathbf{r}, t_k; \sigma) \approx \sum_{i=1}^L \sum_{n=0}^{N_{T_E}} c_i(t_k - n\Delta t) \mathcal{M}_{\mathbf{E}_i}^n(\mathbf{r}, T_E; \sigma), \quad (13)$$

$$\mathbf{B}(\mathbf{r}, t_k; \sigma) \approx \sum_{i=1}^L \sum_{n=0}^{N_{T_B}} c_i(t_k - n\Delta t) \mathcal{M}_{\mathbf{B}_i}^n(\mathbf{r}, T_B; \sigma), \quad (14)$$

where $N_{T_E} = T_E/\Delta t$, $N_{T_B} = T_B/\Delta t$ and

$$\mathcal{M}_{\mathbf{E}_i}^n(\mathbf{r}, T_E; \sigma) = \text{Re} \left\{ \frac{\Delta t}{\pi} \int_0^{\frac{\pi}{\Delta t}} \mathbf{E}_i(\mathbf{r}, \omega; \sigma) e^{-i\omega n \Delta t} d\omega \right\}, \quad n = 1, 2, \dots, N_{T_E} - 1, \quad (15)$$

$$\mathcal{M}_{\mathbf{B}_i}^n(\mathbf{r}, T_B; \sigma) = \text{Re} \left\{ \frac{\Delta t}{\pi} \int_0^{\frac{\pi}{\Delta t}} \mathbf{B}_i(\mathbf{r}, \omega; \sigma) e^{-i\omega n \Delta t} d\omega \right\}, \quad n = 1, 2, \dots, N_{T_B} - 1. \quad (16)$$

134 Expressions for $\mathcal{M}_{\mathbf{E}_i}^0$, $\mathcal{M}_{\mathbf{E}_i}^{N_{T_E}}$ and $\mathcal{M}_{\mathbf{B}_i}^0$, $\mathcal{M}_{\mathbf{B}_i}^{N_{T_B}}$ are more complicated and are pre-
 135 sented in Appendix A of the current paper. A few comments on the latter equations are
 136 relevant at this point.

137 • T_E and T_B significantly differ. As shown by Kruglyakov, Kuvshinov, and Marshalko
 138 (2022) T_E can be taken as small as 15 min for Fennoscandia. As for T_B , it is sev-
 139 eral orders of magnitude larger than T_E (Kruglyakov, Kuvshinov, & Nair, 2022);
 140 specifically T_B should be taken as large as half a year. Note that in this study we
 141 only model the GEF in the region, not the magnetic field. Therefore, only T_E is
 142 relevant for us.

143 • Computation of the integrals in the right-hand side of Equations (15) and (16) is
 144 performed as follows. First, $\mathbf{E}_i(\mathbf{r}, \omega; \sigma)$ and $\mathbf{B}_i(\mathbf{r}, \omega; \sigma)$ are computed at 60 loga-
 145 rithmically spaced frequencies from $3.67 \cdot 10^{-6}$ to 0.054 Hz. Note that for mag-
 146 netic field, modeling at zero frequency is also required (see equation (A4) from Ap-
 147 pendix A). Further, using cubic spline interpolation as applied to calculated $\mathbf{E}_i(\mathbf{r}, \omega; \sigma)$
 148 and $\mathbf{B}_i(\mathbf{r}, \omega; \sigma)$, one can analytically compute the corresponding integrals.

- 149 • Quantities $\mathcal{M}_{\mathbf{E}_i}^n(\mathbf{r}, T_E; \sigma)$ and $\mathcal{M}_{\mathbf{B}_i}^n(\mathbf{r}, T_B; \sigma)$ are time-invariant, and — for the pre-
150 defined set of \mathbf{j}_i and a given conductivity model — are calculated only once, then
151 stored and used when the calculation of $\mathbf{E}(\mathbf{r}, t; \sigma)$ and $\mathbf{B}(\mathbf{r}, t; \sigma)$ is required.
- 152 • One of the key ingredients to make regional EM modeling in Fennoscandia as re-
153 alistic as feasible is a conductivity model of the Earth’s subsurface of the region.
154 The model adopted in this paper comprises a 3-D part and an underlying 1-D con-
155 ductivity profile (Kuvshinov et al., 2021). 3-D part is based on the SMAP model
156 (Korja et al., 2002), covers the area of 2550×2550 km² and consists of three lay-
157 ers of laterally variable conductivity of 10, 20, and 30 km thicknesses; conductiv-
158 ity distributions in these layers are shown in Figure 3. The lateral discretization
159 of the model is 512×512 cells. Note that this model was also exploited in Marshalko
160 et al. (2021) and Kruglyakov, Kuvshinov, and Marshalko (2022). Another note
161 is that computations of electric and magnetic fields in this model (at a given fre-
162 quency) are performed using the scalable 3-D EM forward modeling code PGIEM2G
163 (Kruglyakov & Kuvshinov, 2018) based on a method of volume integral equation
164 with a contracting kernel (Pankratov & Kuvshinov, 2016).
- 165 • As seen from the above equations, GEF computations require specification of SM $\mathbf{j}_i(\mathbf{r})$
166 and estimation of time series of coefficients $c_i(t)$. We address this topic in the next
167 two sections.

168 *2.1.3 GEF modeling using the SECS-based approach*

169 As mentioned in the Introduction, SM $\mathbf{j}_i(\mathbf{r})$ (and corresponding time series of ex-
170 pansion coefficients $c_i(t)$) can be obtained using the following two-step scheme (Kruglyakov,
171 Kuvshinov, & Marshalko, 2022):

- 172 1. Spherical Elementary Current Systems (SECS) method (Vanhamäki & Juusola,
173 2020) is applied to 29-31 October 2003 IMAGE magnetic field data to separate
174 the inducing and induced current systems. The data from all 26 magnetometers
175 were used to perform SECS analysis. Note that IMAGE data for this time inter-
176 val (72 hours) contain several gaps; linear interpolation was used to obtain mag-
177 netic field data in the gaps.
- 178 2. The PCA is applied to the SECS-recovered inducing source resulting in the de-
179 sired SM $\mathbf{j}_i(\mathbf{r}), i = 1, 2, \dots, L$, and time series of the corresponding expansion co-
180 efficients $c_i(t)$. With $L = 34$, we succeeded to describe 99.9% of the inducing source
181 variability.

182 Once $\mathbf{j}_i(\mathbf{r})$ and $c_i(t)$ are derived, the GEF can be computed using Equations (13). Here-
183 inafter we will refer to this two-step approach to specify the source and, consequently,
184 compute the GEF as the SECS-based method.

185 It is important to discuss here one potential drawback of the SECS-based approach
186 to isolate the inducing source (see also Juusola et al. (2020), Section 4.3). Note that this
187 method can be viewed as a regional variant of the Gauss method – the method widely
188 used to separate the inducing (external) and induced (internal) sources on a global scale.
189 If the region of interest is characterized substantially by 3-D conductivity distribution
190 (as in our case) the induced part is inevitably influenced by 3-D effects arising, in par-
191 ticular, from the lateral (for example, land/ocean) conductivity contrasts. Given defi-
192 cient spatial distribution of the IMAGE sites, SECS-based approach precludes an accu-
193 rate description of the induced part affected by localized 3-D effects. Evidently, such im-
194 perfection in induced part description also influences the recovery of the inducing part,
195 at least in terms of $c_i(t)$ recovery.

196 In the next section we discuss an approach to circumvent this issue.

197 **2.1.4 GEF modeling using the conductivity-based approach**

198 Let us first assume that the IMAGE data analysis discussed in the previous sec-
199 tion gives us trustworthy SM $\mathbf{j}_i(\mathbf{r})$. Assume further that the ground 3-D conductivity
200 distribution is known to us at the inducing source construction stage; this is the reason
201 why we call the method discussed in this section the conductivity-based (CB) approach.

With the above assumptions in mind the most adequate way to obtain $c_i(t)$ at a
given time instant is to reuse Equation (14). Specifically, the calculation of $c_i(t)$ at a given
time instant $t_k = k\Delta t$ is performed as follows. Substituting coordinates of IMAGE sites
into Equation (14) and rearranging the terms, we obtain a system of equations to de-
termine $c_i(t_k)$

$$\sum_{i=1}^L c_i(t_k) \mathcal{M}_{\mathbf{B}_i}^0(\mathbf{r}_j, T_B; \sigma) = \mathbf{B}^{obs}(\mathbf{r}_j, t_k) - \sum_{i=1}^L \sum_{n=1}^N c_i(t_k - n\Delta t) \mathcal{M}_{\mathbf{B}_i}^n(\mathbf{r}_j, T_B; \sigma), \quad (17)$$

202 where $N = \min(k-1, N_{T_B})$, $j = 1, 2, \dots, J$, and J is the number of IMAGE sites. The
203 expression (17) represents an overdetermined system of linear equations which is solved
204 by least-square method.

205 This scheme was implemented and validated by Kruglyakov, Kuvshinov, and Nair
206 (2022) who analyzed hourly-mean mid-latitude magnetic field signals of magnetospheric/ionospheric
207 origin. As it is seen from (17), computational loads to obtain $c_i(t_k)$, i.e. for single time
208 instance, are proportional to $L \times N_{T_B}$. In our scenario, $L = 34$, $N_{T_B} = 180 \times 24 \times 60 \times 6$
209 making computational loads to be prohibitively high; recall that the value for $N_T = T_B/\Delta t$
210 is obtained assuming that T_B is taken as half of the year, i.e. $T_B = 180 \times 24 \times 60 \times 60$
211 s, and $\Delta t = 10$ s.

212 Note that the above discussed approaches were developed to perform the near real-
213 time calculations of the GEF (and magnetic field if needed). In this paper we are inter-
214 ested in computing the GEF for the specific event, and, thus, we can exploit an alter-
215 native variant of the CB approach. Noteworthy, this variant has been routinely used for
216 the last two decades to analyse the ground-based signals of magnetospheric origin (Olsen
217 & Kuvshinov, 2004; Püthe & Kuvshinov, 2013a; Püthe et al., 2014; Honkonen et al., 2018;
218 Munch et al., 2020). As applied to our problem setup, this variant of the CB method
219 includes the following steps:

- 220 1. Magnetic field data $\mathbf{B}^{obs}(\mathbf{r}_j, t)$, $j = 1, 2, \dots, J$ recorded at IMAGE sites are con-
221 verted from the time to frequency domain using the fast Fourier Transform (FFT).
222 Note that in our case, $J = 23$; sites Ny Ålesund, Longyearbyen, and Hornsund
223 fall outside the modeling region.
2. At each FFT frequency ω , we estimate $c_i(\omega)$ by solving the over-determined sys-
tem of linear equations

$$\sum_{i=1}^L c_i(\omega) \mathbf{B}_i(\mathbf{r}_j, \omega; \sigma) = \mathbf{B}^{obs}(\mathbf{r}_j, \omega), \quad j = 1, 2, \dots, J, \quad (18)$$

224 by means of the regularized least squares method. Note that FFT frequencies range
225 between $\frac{1}{S}$ and $\frac{1}{2\Delta t}$ where S is the length of the event (72 h).

- 226 3. Time series $c_i(t)$, $i = 1, \dots, L$ are then obtained by means of the inverse FFT of
227 frequency-domain coefficients $c_i(\omega)$.

228 4. Finally, the GEF at a given time instant t_k and location \mathbf{r} is computed using Equa-
 229 tion (13).

230 2.2 GEF modeling using the MT intersite impedance method

231 Although in reality the source of the ground EM field is always laterally variable,
 232 conventional approach to model GEF relies on the plane-wave source assumption. Such
 233 assumption allows researchers to relate the frequency-domain (horizontal) GEF at point
 234 \mathbf{r} with horizontal magnetic field at a base site \mathbf{r}_b through the intersite impedance (Kruglyakov
 235 & Kuvshinov, 2019)

$$\begin{aligned} \mathbf{E}_h(\mathbf{r}, \omega; \sigma) &= \frac{1}{\mu_0} Z(\mathbf{r}, \mathbf{r}_b, \omega; \sigma) \mathbf{B}_h(\mathbf{r}_b, \omega; \sigma), \\ Z(\mathbf{r}, \mathbf{r}_b, \omega; \sigma) &= \begin{pmatrix} Z_{xx} & Z_{xy} \\ Z_{yx} & Z_{yy} \end{pmatrix}. \end{aligned} \quad (19)$$

236 Note that if \mathbf{r} coincides with \mathbf{r}_b , an intersite impedance transforms into a standard 3-D MT
 237 impedance (Berdichevsky & Dmitriev, 2008).

GEF at a given time instant t_k and location \mathbf{r} is then calculated using a numerical
 scheme similar to that described in Section 2.1.2 (cf. Equation 13), namely

$$\mathbf{E}_h(\mathbf{r}, t_k; \sigma) \approx \frac{1}{\mu_0} \sum_{n=0}^{N_{TE}} Z(\mathbf{r}, \mathbf{r}_b, T_E; \sigma) \mathbf{B}_h^{obs}(\mathbf{r}_b, t_k - n\Delta t). \quad (20)$$

238 3 Results

239 3.1 Original current versus PCA-constrained current

Since two approaches discussed in Sections 2.1.3 and 2.1.4 exploit PCA-recovered
 SM, we explore in this section how well the (ionospheric) equivalent current calculated
 using $L = 34$ SM identified by the PCA fits the original equivalent current obtained
 using the SECS technique. Figure 1 demonstrates time series of the aforementioned cur-
 rents above two exemplary sites: Abisko (ABK; latitude: 68.35°N , longitude: 18.82°E)
 and Nurmijärvi (NUR; latitude: 60.5°N , longitude: 24.65°E); their locations are shown
 in Figure 2. One can hardly see the difference between the results. A perfect fit is also
 quantified in terms of high correlation between time series (0.9997), low normalized root-
 mean-square-errors (nRMSE; lower than 0.023), and low maximum absolute differences
 (MAD; lower than 0.041 A/m) for both x (north) and y (east) components of the equiv-
 alent current at each location. Note that nRMSE is defined as follows:

$$\text{nRMSE}(a, b) = \sqrt{\frac{\sum_{i=1}^{N_l} (a_i - b_i)^2}{N_l}} \bigg/ \sqrt{\frac{\sum_{i=1}^{N_l} b_i^2}{N_l}}, \quad (21)$$

240 where a is the ionospheric equivalent current calculated using PCA-recovered SM and
 241 b is the original ionospheric equivalent current, a_i and b_i are elements of these time se-
 242 ries, and N_l is the number of time instants (in our case, $6 \times 60 \times 72$).

243 We conclude from this comparison that spatial structure of the equivalent current
 244 (at least for the considered 72-hour event) is very well explained by $L = 34$ PCA-based
 245 SM, thus supporting the usage of this SM basis in SECS-based and CB approaches.

246 3.2 SECS-based current versus conductivity-based current

247 In this section, we compare equivalent currents obtained using SECS-based and CB
 248 approaches. Figure 2a shows snapshots of the SECS and CB equivalent currents as well

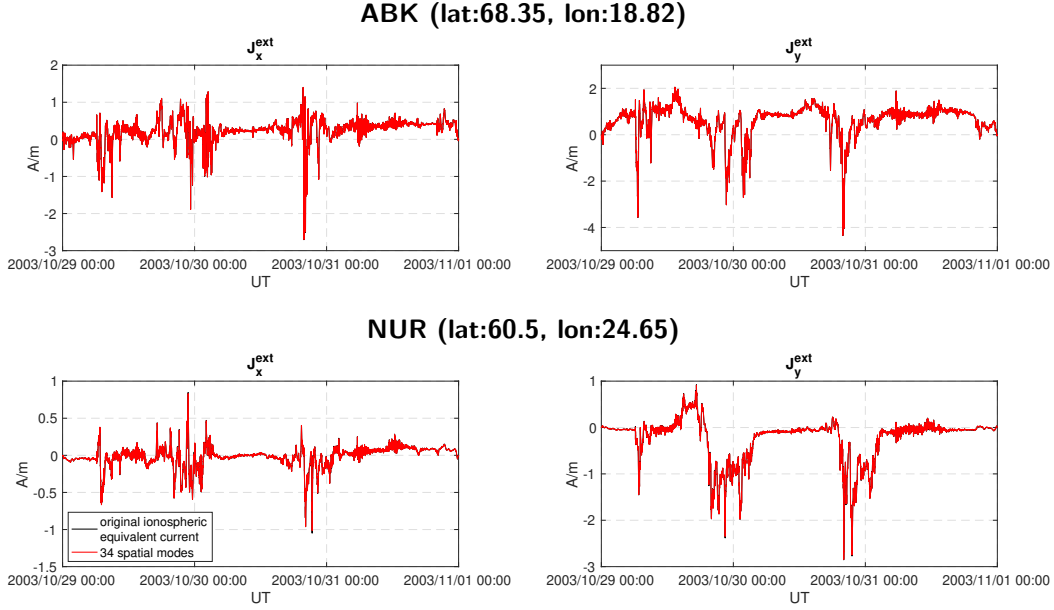


Figure 1. Time series of the original ionospheric equivalent current obtained using the SECS method and ionospheric equivalent current calculated using 34 SM above two exemplary sites: Abisko (ABK) and Nurmijärvi (NUR). The results are in A/m. Left and right panels show x - and y -components of the currents, respectively.

249 as equivalent current's time derivatives above Fennoscandia at 20:08:30 UT, 30 Octo-
 250 ber 2003, — the moment of the largest amplification of GIC in the Finnish natural gas
 251 pipeline during the substorm event, which caused the blackout in Malmö, Sweden. It can
 252 be seen that the overall behavior of equivalent currents is similar. This is also true for
 253 the time derivatives of the equivalent currents. However, the SECS-based source and its
 254 time derivatives have smoother spatial structure compared to CB source. Figure 2b demon-
 255 strates time series of the SECS and CB equivalent currents above ABK and NUR geo-
 256 magnetic observatories. It can be seen that the magnitude of variations is larger in case
 257 of the CB source for NUR. The difference between time series is especially prominent
 258 in case of smaller x -component of the equivalent current. The nRMSE is quite high in
 259 this case — 0.8944. For y -component, the nRMSE is 0.2826. For ABK, good match be-
 260 tween time series of equivalent currents is observed.

261 The detected difference in the recovered equivalent currents will be further assessed
 262 in the next sections by comparing GEF and GIC modeled with the use of different ap-
 263 proaches.

264 3.3 Comparison of GEF modeled by three methods

265 Figures 3a and 3b show snapshots of the magnitude and direction of the GEF in
 266 Fennoscandia modeled with the use of the SECS and CB sources, respectively, at 20:08:30
 267 UT, 30 October 2003. Figure 3c presents the absolute difference between magnitudes of
 268 the GEF demonstrated in Figures 3a and 3b. Figure 3d shows the GEF in the area of
 269 the Finnish natural gas pipeline modeled using the CB equivalent current at 20:08:30
 270 UT, 30 October 2003. Finally, Figures 3e-g demonstrate conductivity distribution in three
 271 layers of the 3-D model that we use in our simulations. It is clear that the overall be-
 272 havior of the GEF obtained with the use of the considered sources is very similar. How-
 273 ever, it can be seen that differences in magnitudes of the GEF reach over 8300 mV/km

Table 1. Correlation coefficients, normalized root mean square errors, and maximum absolute differences (in mV/km) between GEF obtained using SECS, CB and MT approaches at Abisko (ABK) and Nurmijärvi (NUR) geomagnetic observatories, Mäntsälä (MAN) GIC recording point, and Point X located 0.5° north of MAN. In case of MAN and Point X, MT results are obtained with the use of magnetic field data observed at NUR.

	ABK	NUR	MAN	Point X
$\text{corr}(E_{x,\text{SECS}}, E_{x,\text{CB}})$	0.9634	0.8588	0.8565	0.8424
$\text{corr}(E_{x,\text{MT}}, E_{x,\text{CB}})$	0.8905	0.9254	0.9344	0.9226
$\text{corr}(E_{y,\text{SECS}}, E_{y,\text{CB}})$	0.9778	0.9288	0.9339	0.9476
$\text{corr}(E_{y,\text{MT}}, E_{y,\text{CB}})$	0.9416	0.9519	0.9542	0.9522
$\text{nRMSE}(E_{x,\text{SECS}}, E_{x,\text{CB}})$	0.2776	0.5123	0.5164	0.5409
$\text{nRMSE}(E_{x,\text{MT}}, E_{x,\text{CB}})$	0.8216	0.4508	0.4136	0.4099
$\text{nRMSE}(E_{y,\text{SECS}}, E_{y,\text{CB}})$	0.2307	0.3802	0.3692	0.3523
$\text{nRMSE}(E_{y,\text{MT}}, E_{y,\text{CB}})$	0.6629	0.558	0.5435	0.4623
$\text{MAD}(E_{x,\text{SECS}}, E_{x,\text{CB}})$	401	2137.3	1366.1	256.4
$\text{MAD}(E_{x,\text{MT}}, E_{x,\text{rec}})$	927.6	1999.9	1114.3	166.3
$\text{MAD}(E_{y,\text{SECS}}, E_{y,\text{CB}})$	305.5	506.3	490.8	350
$\text{MAD}(E_{y,\text{MT}}, E_{y,\text{CB}})$	961.4	745.9	709.4	293.1

274 at this particular time instant at the Norwegian coastline (see Figure 3c). Besides, the
 275 behavior of the GEF in the region is complex; the magnitude of the GEF can decrease
 276 or increase many times over short distances due to lateral variations of conductivity, es-
 277 pecially at the ocean coast as it is demonstrated in Figures 3a-b.

278 Figure 4 shows the snapshots of the GEF across Fennoscandia (left figures) and in
 279 the area of the Finnish natural gas pipeline (right figures) at two moments of maximum
 280 GIC amplification at Mäntsälä, which occurred during the initial phase of the Halloween
 281 geomagnetic storm: 06:57:30 and 07:27:00 UT, 29 October 2003.

282 We also compare GEF modeled with the use of three approaches at several loca-
 283 tions: ABK, NUR, MAN pipeline recording point (latitude: 60.6°N , longitude: 25.2°E)
 284 and Point X, which is located 0.5° north of MAN (cf. Figures 5-8). It is worth mention-
 285 ing that even though NUR, MAN, and Point X are located very close to each other (about
 286 32 km apart in case of NUR and MAN and about 56 km in case of MAN and Point X),
 287 the magnitude of the GEF variations at these three sites is very different. The highest
 288 GEF values are observed at NUR, which is located above a resistive structure and close
 289 to a border of conductivity contrast (see Figure 3e). Point X is located above a more con-
 290 ductive structure. That is why GEF values are smaller at this site.

291 We further quantify the difference between modeled GEF in terms of correlation
 292 coefficients, nRMSE, and MAD in Table 1. Note that MAD between x -components of
 293 the GEF induced by the SECS and CB source as well as those between x -components
 294 of the GEF obtained using CB source and MT impedance method are quite large at NUR
 295 and MAN due to the fact that GEF values at this locations are also large at the moment
 296 of maximum GEF amplification. MAD are significantly smaller in case of Point X. How-
 297 ever, the nRMSE between x -components of the GEF induced by SECS and CB source
 298 at NUR, MAN, and Point X are practically equal.

299

3.4 Comparison of modeled and observed GIC

300

301

We calculate GIC based on the GEF modeled via three methods discussed above and compare them with GIC observed at the MAN natural gas pipeline recording point.

It was previously demonstrated by Viljanen et al. (2006) that GIC at MAN can be reproduced accurately enough based on the horizontal electric field data using the following expression:

$$\text{GIC}(t) = aE_x(t) + bE_y(t), \quad (22)$$

302

303

304

305

306

where coefficients a and b depend only on the topology and resistances of the pipeline system. In their study, Viljanen et al. (2006) exploited parameters determined by Pulkkinen et al. (2001): $a = -70 \text{ A}\cdot\text{km}/\text{V}$ and $b = 88 \text{ A}\cdot\text{km}/\text{V}$. It should be noted that above expression is a simplification and it assumes that the GEF along the pipeline is spatially uniform.

307

308

309

310

311

312

313

314

315

316

317

318

319

Figure 9a demonstrates the comparison of observed GIC and GIC calculated based on the GEF simulated at MAN with the use of the CB source. Note that modeled GIC is scaled by a factor of 4.51 in the figure. The iteratively reweighted least squares algorithm (Holland & Welsch, 1977) was used to estimate this factor. Note that in the study of Dimmock et al. (2019) who carried out 3-D GEF and GIC modeling in the Fennoscandian region due to 7-8 September 2017 geomagnetic storm, GIC calculated based on Pulkkinen et al. (2001) parameters and GEF simulated in the SMAP conductivity model was also scaled by a factor of 4. Dimmock et al. (2019) point out that conductivities in the model adopted by Viljanen et al. (2006) are significantly larger than those in the SMAP model. Figures 9b and 9c provide a closer look on time intervals 06:00:00-08:00:00 UT, 29 October 2003 (the initial phase of the Halloween geomagnetic storm, when the largest GIC value was observed at MAN), and 19:00:00-21:00:00 UT, 30 October 2003 (the substorm event, which caused the blackout in Malmö, Sweden).

320

321

322

When calculating GIC based on the GEF modeled with the SECS-based source and MT method, scaling factors should also be applied. The scaling factors estimated via the iteratively reweighted least squares algorithm are 4.68 and 5.39, correspondingly.

323

324

325

326

327

328

As it was demonstrated in Section 3.3, GEF values at Point X are significantly smaller than those at MAN due to the fact that Point X is located on a more conductive basement. Figure 9d demonstrates the comparison of observed GIC and GIC calculated based on the GEF simulated at Point X with the use of the CB source. Modeled GIC are not scaled in this figure. It is clear that simulated GIC variations are of the same order of magnitude as observed ones.

329

330

331

332

333

Table 2 presents correlation coefficients, nRMSE, and MAD between observed GIC and GIC calculated based on the GEF modeled with the use of the three discussed methods. The values are demonstrated for GIC calculated both at MAN and Point X locations. It can be seen that the highest correlation between modeled and observed GIC is achieved with the use of the CB source.

334

4 Concluding Remarks

335

336

337

338

339

340

341

In this paper, we perform rigorous 3-D GEF modeling in Fennoscandia for three days of the Halloween geomagnetic storm (29-31 October 2003). To explore the influence of the inducing source model on 3-D GEF simulations, we consider three different approaches to approximate the source. Noteworthy, all methods exploit the same IMAGE magnetic field data to simulate the GEF, rely on the same high-resolution 3-D conductivity model of the region (SMAP, Korja et al. (2002)), and use the same forward problem engine (Kruglyakov & Kuvshinov, 2018).

Table 2. Correlation coefficients, normalized root mean square errors, and maximum absolute differences (in A) between modeled and observed GIC at the Mäntsälä (MAN) pipeline recording point and Point X located 0.5° north of MAN. Note that modeled GIC at MAN are scaled by factors of 4.68 (using SECS source), 5.39 (using MT method), and 4.51 (using CB source). At Point X, GIC are not scaled.

	MAN	Point X
$\text{corr}(\text{GIC}_{\text{SECS}}, \text{GIC}_{\text{obs}})$	0.7729	0.724
$\text{corr}(\text{GIC}_{\text{MT}}, \text{GIC}_{\text{obs}})$	0.8857	0.7951
$\text{corr}(\text{GIC}_{\text{CB}}, \text{GIC}_{\text{obs}})$	0.9026	0.8094
$\text{nRMSE}(\text{GIC}_{\text{SECS}}, \text{GIC}_{\text{obs}})$	0.6345	0.7108
$\text{nRMSE}(\text{GIC}_{\text{MT}}, \text{GIC}_{\text{obs}})$	0.4647	0.8198
$\text{nRMSE}(\text{GIC}_{\text{CB}}, \text{GIC}_{\text{obs}})$	0.4306	0.6342
$\text{MAD}(\text{GIC}_{\text{SECS}}, \text{GIC}_{\text{obs}})$	40.3	52.7
$\text{MAD}(\text{GIC}_{\text{MT}}, \text{GIC}_{\text{obs}})$	28.8	64.8
$\text{MAD}(\text{GIC}_{\text{CB}}, \text{GIC}_{\text{obs}})$	29.1	56.4

342 Within the first two approaches, the source varies laterally and is factorized from
 343 the original SECS-recovered source (Vanhamäki & Juusola, 2020) by spatial modes (SM)
 344 and respective expansion coefficients. In both approaches, the SM are the same and ob-
 345 tained following the two-step numerical scheme introduced by Kruglyakov, Kuvshinov,
 346 and Marshalko (2022). The difference between methods lies in the calculation of the ex-
 347 pansion coefficients; in the second approach, which we call “conductivity-based”, the ex-
 348 pansion coefficients are obtained by taking the conductivity distribution of the earth into
 349 account. Within the third approach, the GEF is calculated by implementing the time-
 350 domain realization of the MT intersite impedance method.

351 We modeled GIC at the MAN Finnish natural gas pipeline recording site based on
 352 the GEF obtained with the use of three aforementioned modeling approaches and com-
 353 pared results with GIC observed there. We conclude that for all considered methods, the
 354 correlation between modeled and observed GIC is high. The highest correlation with GIC
 355 recordings and the lowest nRMSE is achieved with the use of the CB source. However,
 356 when calculating GIC based on the GEF simulated at MAN, their values appear to be
 357 overestimated 4–6 times in case of all modeling techniques. Similar results were obtained
 358 by Dimmock et al. (2019) who calculated GIC at MAN based the GEF computed in the
 359 SMAP model during 7–8 September 2017 geomagnetic storm. When calculating GIC on
 360 the basis of the GEF at a point located 0.5° north of MAN (and on a significantly more
 361 conductive basement), resulting GIC have the same order of magnitude as observed ones.
 362 As this example demonstrates, the ground conductivity has a crucial role in estimating
 363 the GEF. Especially challenging are regions with sharp gradients of the near-surface con-
 364 ductivity. We also stress that in contrast to the spatially highly variable ground conduc-
 365 tivity, the equivalent ionospheric currents and their time derivatives are relatively smooth.
 366 Thus, most of the lateral variation of the GEF arises from the ground conductivity.

367 For GIC calculation in this study, we used a simplified method, which assumes that
 368 the GEF along the pipeline is spatially uniform. One can argue that this approximation
 369 is too rough taking into account that our modeling results demonstrate large differences
 370 between GEF values at different sites in the pipeline area (see Figures 3d and 6–8). Cal-
 371 culation of the actual GIC in technological networks is an engineering task, which can
 372 be performed with a significantly higher level of accuracy by companies operating these
 373 networks and possessing all the necessary information about their configurations and pa-

rameters. Moreover, the information about changes in configurations of technological systems over the years is required to model GIC properly during a particular time interval. That is why in this study, we limit ourselves to using this simplified GIC modeling method, with the help of which reasonable modeling results were previously obtained by Viljanen et al. (2006). We also share our GEF simulation results through an open-access repository (Marshalko et al., 2022). With the help of these data, companies operating technological systems in Fennoscandia will be able to assess the potential hazard to these systems from space weather.

Concerning future studies, our results of the Halloween storm serve as an explicit point of comparison. Using the same ground conductivity model, but different geomagnetic field input, we can quantify the magnitude of other events with respect to the Halloween storm. Of special interest is a recent reproduction of the Carrington storm by Blake et al. (2021) and the simulation of a sudden storm commencement due to an extreme solar wind shock (Welling et al., 2021).

Another topic for future activity is updating the 3-D conductivity model of Fennoscandia, which is to be based on a multi-scale 3-D inversion of a significant amount of new MT data collected in the region in the framework of various goal-oriented MT projects. Note that the biggest uncertainty in the GEF and GIC modeling arises due to incompleteness of the conductivity model. In a recent study, Love et al. (2022) considered the famous magnetic storm in March 1989. They presented maps of reported GIC impacts in the contiguous United States (CONUS) power grids and compared their occurrence to the peak values of the GEF based on empirical MT impedances. There is a clear correspondence between the locations of GIC impacts and high GEF values. As Love et al. (2022) point out, geomagnetic variations tend to decrease with decreasing geomagnetic latitude. This is also seen in geoelectric hazard maps. However, the hazard across CONUS is much more prominently organized by the surface impedance, i.e. the ground conductivity. This emphasises the need for using as accurate information on the earth conductivity as possible.

Finally, the ongoing research aims to further develop the conductivity-based approach to enable its real-time implementation.

5 Open Research

Modeled GEF data are available at <https://doi.org/10.5281/zenodo.7385880> under CC BY 4.0. The SMAP model (Korja et al., 2002) is publicly available via the EPOS portal: http://mt.bgs.ac.uk/EPOSMT/2019/MOD/EPOSMT2019_3D.mod.json. PGIEM2G 3-D EM forward modeling code is openly available under GPLv2 via Gitlab: <https://gitlab.com/m.kruglyakov/PGIEM2G>.

Acknowledgments

EM and AV were supported by grants 314670 and 339329 from the Academy of Finland. MK was supported by the New Zealand Ministry of Business, Innovation, & Employment through Endeavour Fund Research Programme contract UOOX2002. AK was supported in the framework of Swarm DISC activities, funded by ESA contract no. 4000109587, with the support from EO Science for Society. We thank the institutes that maintain the IMAGE Magnetometer Array: Tromsø Geophysical Observatory of UiT, the Arctic University of Norway (Norway), Finnish Meteorological Institute (Finland), Institute of Geophysics Polish Academy of Sciences (Poland), GFZ German Research Center for Geosciences (Germany), Geological Survey of Sweden (Sweden), Swedish Institute of Space Physics (Sweden), Sodankylä Geophysical Observatory of the University of Oulu (Finland), and Polar Geophysical Institute (Russia). We acknowledge Gasum Oy for long-term collaboration in GIC studies of the Finnish natural gas pipeline.

References

423

424

425

426

427

428

429

430

431

432

433

434

435

436

437

438

439

440

441

442

443

444

445

446

447

448

449

450

451

452

453

454

455

456

457

458

459

460

461

462

463

464

465

466

467

468

469

470

471

472

473

474

475

476

- Berdichevsky, M. N., & Dmitriev, V. I. (2008). *Models and methods of magnetotellurics*. Springer, Berlin, Heidelberg. doi: 10.1007/978-3-540-77814-1
- Blake, S. P., Pulkkinen, A., Schuck, P. W., Glocer, A., Oliveira, D. M., Welling, D. T., ... Quaresima, G. (2021). Recreating the horizontal magnetic field at Colaba during the Carrington event with geospace simulations. *Space Weather*, 19(5), e2020SW002585. doi: 10.1029/2020SW002585
- Dimmock, A. P., Rosenqvist, L., Hall, J.-O., Viljanen, A., Yordanova, E., Honkonen, I., ... Sjöberg, E. C. (2019). The GIC and geomagnetic response over Fennoscandia to the 7-8 September 2017 geomagnetic storm. *Space Weather*, 17(7), 989–1010. doi: 10.1029/2018SW002132
- Egbert, G. D., Alken, P., Maute, A., Zhang, H., & Richmond, A. D. (2021). Modeling diurnal variation magnetic fields for mantle induction studies. *Geophysical Journal International*. doi: 10.1093/gji/ggaa533
- Grayver, A., Kuvshinov, A., & Werthmüller, D. (2021). Time-domain modeling of 3-D Earth's and planetary electromagnetic induction effect in ground and satellite observations. *Journal of Geophysical Research: Space Physics*, e2020JA028672. doi: 10.1029/2020JA028672
- Guzavina, M., Grayver, A., & Kuvshinov, A. (2019). Probing upper mantle electrical conductivity with daily magnetic variations using global to local transfer functions. *Geophysical Journal International*, 219(3), 2125–2147. doi: 10.1093/gji/ggz412
- Holland, P. W., & Welsch, R. E. (1977). Robust regression using iteratively reweighted least-squares. *Communications in Statistics - Theory and Methods*, 6(9), 813–827. doi: 10.1080/03610927708827533
- Honkonen, I., Kuvshinov, A., Rastätter, L., & Pulkkinen, A. (2018). Predicting global ground geoelectric field with coupled geospace and three-dimensional geomagnetic induction models. *Space Weather*, 16(8), 1028–1041. doi: 10.1029/2018SW001859
- Ivannikova, E., Kruglyakov, M., Kuvshinov, A., Rastätter, L., & Pulkkinen, A. (2018). Regional 3-D modeling of ground electromagnetic field due to realistic geomagnetic disturbances. *Space Weather*, 16(5), 476–500. doi: 10.1002/2017SW001793
- Juusola, L., Vanhamäki, H., Viljanen, A., & Smirnov, M. (2020). Induced currents due to 3D ground conductivity play a major role in the interpretation of geomagnetic variations. *Annales Geophysicae*, 38(5), 983–998. doi: 10.5194/angeo-38-983-2020
- Kelbert, A. (2020). The role of global/regional Earth conductivity models in natural geomagnetic hazard mitigation. *Surveys in Geophysics*, 41, 115–166. doi: 10.1007/s10712-019-09579-z
- Korja, T., Engels, M., Zhamaletdinov, A. A., Kovtun, A. A., Palshin, N. A., Smirnov, M. Y., ... BEAR Working Group (2002). Crustal conductivity in Fennoscandia – a compilation of a database on crustal conductance in the Fennoscandian Shield. *Earth, Planets and Space*, 54, 535–558. doi: 10.1186/BF03353044
- Kruglyakov, M., & Kuvshinov, A. (2018). Using high-order polynomial basis in 3-D EM forward modeling based on volume integral equation method. *Geophysical Journal International*, 213(2), 1387–1401. doi: 10.1093/gji/ggy059
- Kruglyakov, M., & Kuvshinov, A. (2019). 3-D inversion of MT impedances and inter-site tensors, individually and jointly. New lessons learnt. *Earth, Planets and Space*, 71(1), 1–9. doi: 10.1186/s40623-018-0972-8
- Kruglyakov, M., Kuvshinov, A., & Marshalko, E. (2022). Real-time 3-D modeling of the ground electric field due to space weather events. A concept and its validation. *Space Weather*, 20(4), e2021SW002906. doi: 10.1029/2021SW002906

- 477 Kruglyakov, M., Kuvshinov, A., & Nair, M. (2022). A proper use of the adja-
 478 cent land-based observatory magnetic field data to account for the geomag-
 479 netic disturbances during offshore directional drilling. *Space Weather*. doi:
 480 10.1029/2022SW003238
- 481 Kuvshinov, A., Grayver, A., Tøffner-Clausen, L., & Olsen, N. (2021). Probing 3-D
 482 electrical conductivity of the mantle using 6 years of Swarm, CryoSat-2 and
 483 observatory magnetic data and exploiting matrix Q-responses approach. *Earth,*
 484 *Planets and Space*, *73*, 67. doi: 10.1186/s40623-020-01341-9
- 485 Lehtinen, M., & Pirjola, R. J. (1985). Currents produced in earthed conductor net-
 486 works by geomagnetically-induced electric fields. *Annales Geophysicae*, *3*, 479-
 487 484.
- 488 Love, J. J., Lucas, G. M., Rigler, E. J., Murphy, B. S., Kelbert, A., & Bedrosian,
 489 P. A. (2022). Mapping a magnetic superstorm: March 1989 geoelectric haz-
 490 ards and impacts on United States power systems. *Space Weather*, *20*(5),
 491 e2021SW003030. doi: 10.1029/2021SW003030
- 492 Marshalko, E., Kruglyakov, M., Kuvshinov, A., Juusola, L., Kwagala, N. K.,
 493 Sokolova, E., & Pilipenko, V. (2021). Comparing three approaches to
 494 the inducing source setting for the ground electromagnetic field modeling
 495 due to space weather events. *Space Weather*, *19*(2), e2020SW002657. doi:
 496 10.1029/2020SW002657
- 497 Marshalko, E., Kruglyakov, M., Kuvshinov, A., Murphy, B. S., Rastätter, L., Ng-
 498 wira, C., & Pulkkinen, A. (2020). Exploring the influence of lateral con-
 499 ductivity contrasts on the storm time behavior of the ground electric field
 500 in the eastern United States. *Space Weather*, *18*(3), e2019SW002216. doi:
 501 10.1029/2019SW002216
- 502 Marshalko, E., Kruglyakov, M., Kuvshinov, A., & Viljanen, A. (2022, December).
 503 *Dataset for "Rigorous 3-D modeling of the ground electric field in Fennoscandia during the Halloween geomagnetic storm", Marshalko et al. (2023), Space*
 504 *Weather*. Zenodo. doi: 10.5281/zenodo.7385880
- 506 Munch, F. D., Grayver, A. V., Guzavina, M., Kuvshinov, A. V., & Khan, A. (2020).
 507 Joint inversion of daily and long-period geomagnetic transfer functions re-
 508 veals lateral variations in mantle water content. *Geophys. Res. Lett.*, *47*(10),
 509 e2020GL087222. doi: 10.1029/2020GL087222
- 510 Myllys, M., Viljanen, A., Rui, O. A., & Ohnstad, T. M. (2014). Geomagnetically
 511 induced currents in Norway: the northernmost high-voltage power grid in the
 512 world. *J. Space Weather Space Clim.*, *4*, A10. doi: 10.1051/swsc/2014007
- 513 Olsen, N., & Kuvshinov, A. (2004). Modelling the ocean effect of geomagnetic
 514 storms. *Earth, Planets and Space*, *56*, 525-530.
- 515 Pankratov, O., & Kuvshinov, A. (2016). Applied mathematics in EM stud-
 516 ies with special emphasis on an uncertainty quantification and 3-D inte-
 517 gral equation modelling. *Surveys in Geophysics*, *37*(1), 109-147. doi:
 518 10.1007/s10712-015-9340-4
- 519 Pirjola, R. J., Boteler, D. H., Tuck, L., & Marsal, S. (2022). The Lehtinen–Pirjola
 520 method modified for efficient modelling of geomagnetically induced currents
 521 in multiple voltage levels of a power network. *Annales Geophysicae*, *40*(2),
 522 205–215. doi: 10.5194/angeo-40-205-2022
- 523 Pulkkinen, A., Bernabeu, E., Thomson, A., Viljanen, A., Pirjola, R., Boteler, D.,
 524 ... MacAlester, M. (2017). Geomagnetically induced currents: Science, en-
 525 gineering, and applications readiness. *Space Weather*, *15*(7), 828–856. doi:
 526 10.1002/2016SW001501
- 527 Pulkkinen, A., Lindahl, S., Viljanen, A., & Pirjola, R. (2005). Geomagnetic storm
 528 of 29–31 October 2003: Geomagnetically induced currents and their relation
 529 to problems in the Swedish high-voltage power transmission system. *Space*
 530 *Weather*, *3*(8), S08C03. doi: 10.1029/2004SW000123
- 531 Pulkkinen, A., Viljanen, A., Pajunpää, K., & Pirjola, R. (2001). Recordings

- 532 and occurrence of geomagnetically induced currents in the Finnish natural
 533 gas pipeline network. *Journal of Applied Geophysics*, 48(4), 219–231. doi:
 534 10.1016/S0926-9851(01)00108-2
- 535 Püthe, C., & Kuvshinov, A. (2013a). Determination of the 3-D distribution of elec-
 536 trical conductivity in Earth’s mantle from *Swarm* satellite data: Frequency
 537 domain approach based on inversion of induced coefficients. *Earth, Planets and*
 538 *Space*, 65, 1247–1256.
- 539 Püthe, C., & Kuvshinov, A. (2013b). Towards quantitative assessment of the hazard
 540 from space weather. Global 3-D modellings of the electric field induced by a
 541 realistic geomagnetic storm. *Earth, Planets and Space*, 65, 1017–1025. doi:
 542 10.5047/eps.2013.03.003
- 543 Püthe, C., Kuvshinov, A., & Olsen, N. (2014). Handling complex source structures
 544 in global EM induction studies: From C-responses to new arrays of transfer
 545 functions. *Geophys. J. Int.*. doi: 10.1093/gji/ggu027
- 546 Rosenqvist, L., & Hall, J. O. (2019). Regional 3-D modeling and verification of ge-
 547 omagnetically induced currents in Sweden. *Space Weather*, 17(1), 27–36. doi:
 548 10.1029/2018SW002084
- 549 Sun, J., & Egbert, G. D. (2012). Spherical decomposition of electromagnetic fields
 550 generated by quasi-static currents. *GEM - International Journal on Geomathe-*
 551 *matics*, 3(2), 279–295. doi: 10.1007/s13137-012-0039-0
- 552 Tanskanen, E. I. (2009). A comprehensive high-throughput analysis of sub-
 553 storms observed by IMAGE magnetometer network: Years 1993–2003 ex-
 554 amined. *Journal of Geophysical Research: Space Physics*, 114(A5). doi:
 555 10.1029/2008JA013682
- 556 Vanhamäki, H., & Juusola, L. (2020). Introduction to Spherical Elementary Current
 557 Systems. In M. W. Dunlop & H. Lühr (Eds.), *Ionospheric multi-spacecraft*
 558 *analysis tools: Approaches for deriving ionospheric parameters* (pp. 5–33).
 559 Cham: Springer International Publishing. doi: 10.1007/978-3-030-26732-2_2
- 560 Viljanen, A., & Pirjola, R. (1994). Geomagnetically induced currents in the Finnish
 561 high-voltage power system. A geophysical review. *Surv. Geophys.*, 15, 383–408.
 562 doi: 10.1007/BF00665999
- 563 Viljanen, A., Pirjola, R., Prácer, E., Katkalov, J., & Wik, M. (2014). Ge-
 564 omagnetically induced currents in Europe - Modelled occurrence in a
 565 continent-wide power grid. *J. Space Weather Space Clim.*, 4, A09. doi:
 566 10.1051/swsc/2014006
- 567 Viljanen, A., Pulkkinen, A., Pirjola, R., Pajunpää, K., Posio, P., & Koistinen, A.
 568 (2006). Recordings of geomagnetically induced currents and a nowcasting ser-
 569 vice of the Finnish natural gas pipeline system. *Space Weather*, 4(10). doi:
 570 10.1029/2006SW000234
- 571 Wei, L. H., Homeier, N., & Gannon, J. L. (2013). Surface electric fields for North
 572 America during historical geomagnetic storms. *Space Weather*, 11(8), 451–462.
 573 doi: 10.1002/swe.20073
- 574 Welling, D. T., Love, J. J., Rigler, E. J., Oliveira, D. M., Komar, C. M., & Morley,
 575 S. K. (2021). Numerical simulations of the geospace response to the arrival
 576 of an idealized perfect interplanetary coronal mass ejection. *Space Weather*,
 577 19(2), e2020SW002489. doi: 10.1029/2020SW002489
- 578 Zenhausern, G., Kuvshinov, A., Guzavina, M., & Maute, A. (2021). Towards prob-
 579 ing Earth’s upper mantle with daily magnetic field variations: exploring a
 580 physics-based parametrization of the source. *Earth, Planets and Space*, 73,
 581 136. doi: 10.1186/s40623-021-01455-8

582 Appendix A Expressions for $\mathcal{M}_{\mathbf{E}_i}^n$, $\mathcal{M}_{\mathbf{B}_i}^n$

583 The derivation of expressions for $\mathcal{M}_{\mathbf{E}_i}^n$ and $\mathcal{M}_{\mathbf{B}_i}^n$ is presented in Kruglyakov, Ku-
 584 vshinov, and Marshalko (2022) and Kruglyakov, Kuvshinov, and Nair (2022) for elec-

585 tric and magnetic fields, correspondingly. Even though the same technique is used in both
 586 papers, the notation and final form of expressions are different. Thus, to avoid readers'
 587 confusion, we present the expressions for $\mathcal{M}_{\mathbf{E}_i}^n$ and $\mathcal{M}_{\mathbf{B}_i}^n$ in similar closed forms.

As already discussed in Section 2.1.2, the expressions for $\mathcal{M}_{\mathbf{E}_i}^n$ and $\mathcal{M}_{\mathbf{B}_i}^n$ for $n = 1, 2, \dots, N_{T_E} - 1, N_{T_B} - 1$ are the following

$$\mathcal{M}_{\mathbf{E}_i}^n(\mathbf{r}, T_E; \sigma) = \operatorname{Re} \left\{ \frac{\Delta t}{\pi} \int_0^{\frac{\pi}{\Delta t}} \mathbf{E}_i(\mathbf{r}, \omega; \sigma) e^{-i\omega n \Delta t} d\omega \right\}, \quad n = 1, 2, \dots, N_{T_E} - 1, \quad (\text{A1})$$

$$\mathcal{M}_{\mathbf{B}_i}^n(\mathbf{r}, T_B; \sigma) = \operatorname{Re} \left\{ \frac{\Delta t}{\pi} \int_0^{\frac{\pi}{\Delta t}} \mathbf{B}_i(\mathbf{r}, \omega; \sigma) e^{-i\omega n \Delta t} d\omega \right\}, \quad n = 1, 2, \dots, N_{T_B} - 1. \quad (\text{A2})$$

At the same time, for $n = 0, N_{T_E}, N_{T_B}$ the expressions are

$$\begin{aligned} \mathcal{M}_{\mathbf{E}_i}^0(\mathbf{r}_s, T_E; \sigma) &= -\mathcal{L}_{\mathbf{E}_i}(\mathbf{r}_s, T_E; \sigma) - \sum_{k=1}^{N_{T_E}-1} \mathcal{M}_{\mathbf{E}_i}^k(\mathbf{r}_s, T_E; \sigma) \left(1 - \frac{k}{N_{T_E}}\right), \\ \mathcal{M}_{\mathbf{E}_i}^{N_{T_E}}(\mathbf{r}_s, T_E; \sigma) &= \mathcal{L}_{\mathbf{E}_i}(\mathbf{r}_s, T_E; \sigma) - \sum_{k=1}^{N_{T_E}-1} \mathcal{M}_{\mathbf{E}_i}^k(\mathbf{r}_s, T_E; \sigma) \frac{k}{N_{T_E}}, \end{aligned} \quad (\text{A3})$$

$$\begin{aligned} \mathcal{M}_{\mathbf{B}_i}^0(\mathbf{r}_s, T_B; \sigma) &= -\mathcal{L}_{\mathbf{B}_i}(\mathbf{r}_s, T_B; \sigma) - \sum_{k=1}^{N_{T_B}-1} \mathcal{M}_{\mathbf{B}_i}^k(\mathbf{r}_s, T_B; \sigma) \left(1 - \frac{k}{N_{T_B}}\right) \\ &\quad + \operatorname{Re} \mathbf{B}_i(\mathbf{r}_s, \omega; \sigma)|_{\omega=0}, \\ \mathcal{M}_{\mathbf{B}_i}^{N_{T_B}}(\mathbf{r}_s, T_B; \sigma) &= \mathcal{L}_{\mathbf{B}_i}(\mathbf{r}_s, T_B; \sigma) - \sum_{k=1}^{N_{T_B}-1} \mathcal{M}_{\mathbf{B}_i}^k(\mathbf{r}_s, T_B; \sigma) \frac{k}{N_{T_B}}. \end{aligned} \quad (\text{A4})$$

588 It is worth stressing here that unlike (A3), (A4) contains an additional term $\operatorname{Re} \mathbf{B}_i(\mathbf{r}_s, \omega; \sigma)|_{\omega=0}$
 589 for $n = 0$ since the magnetic field is not necessarily zero for $\omega = 0$.

Functions $\mathcal{L}_{\mathbf{E}_i}(\mathbf{r}_s, T_E; \sigma)$ and $\mathcal{L}_{\mathbf{B}_i}(\mathbf{r}_s, T_B; \sigma)$ have the following form:

$$\mathcal{L}_{\mathbf{E}_i}(\mathbf{r}_s, T_E; \sigma) = \frac{1}{T_E} \int_0^{T_E} \tau \mathbf{E}_i(\mathbf{r}_s, \tau; \sigma) d\tau, \quad (\text{A5})$$

$$\mathcal{L}_{\mathbf{B}_i}(\mathbf{r}_s, T_B; \sigma) = \frac{1}{T_B} \int_0^{T_B} \tau \mathbf{B}_i(\mathbf{r}_s, \tau; \sigma) d\tau. \quad (\text{A6})$$

590 The numerical method to compute integrals (A5) and (A6) is described in Appendix C
 591 of Kruglyakov, Kuvshinov, and Marshalko (2022). Note that although both $\mathcal{L}_{\mathbf{E}_i}(\mathbf{r}_s, T_E; \sigma)$
 592 and $\mathcal{L}_{\mathbf{B}_i}(\mathbf{r}_s, T_B; \sigma)$ vanish as $T_E, T_B \rightarrow \infty$, they decay too slowly to be neglected for
 593 specified values of T_E, T_B .

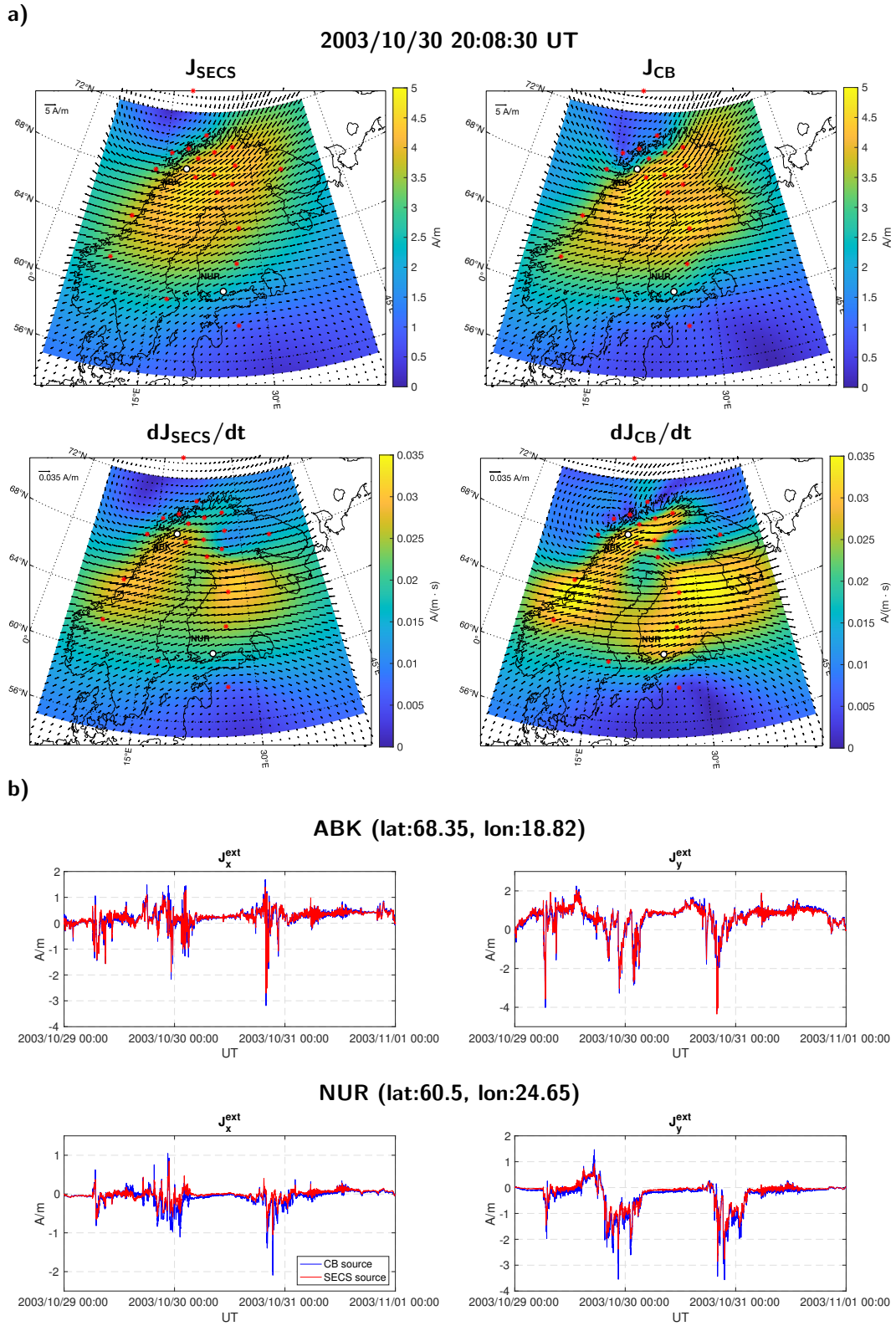


Figure 2. (a) Snapshots of the magnitude and direction of the SECS and CB equivalent currents and equivalent currents' time derivatives above Fennoscandia at 20:08:30 UT, 30 October 2003. IMAGE sites are marked with red asterisks and white circles. (b) Time series of the SECS and CB ionospheric equivalent currents above Abisko (ABK) and Nurmijärvi (NUR) geomagnetic observatories. Left and right panels show x - and y -components of the currents, respectively.

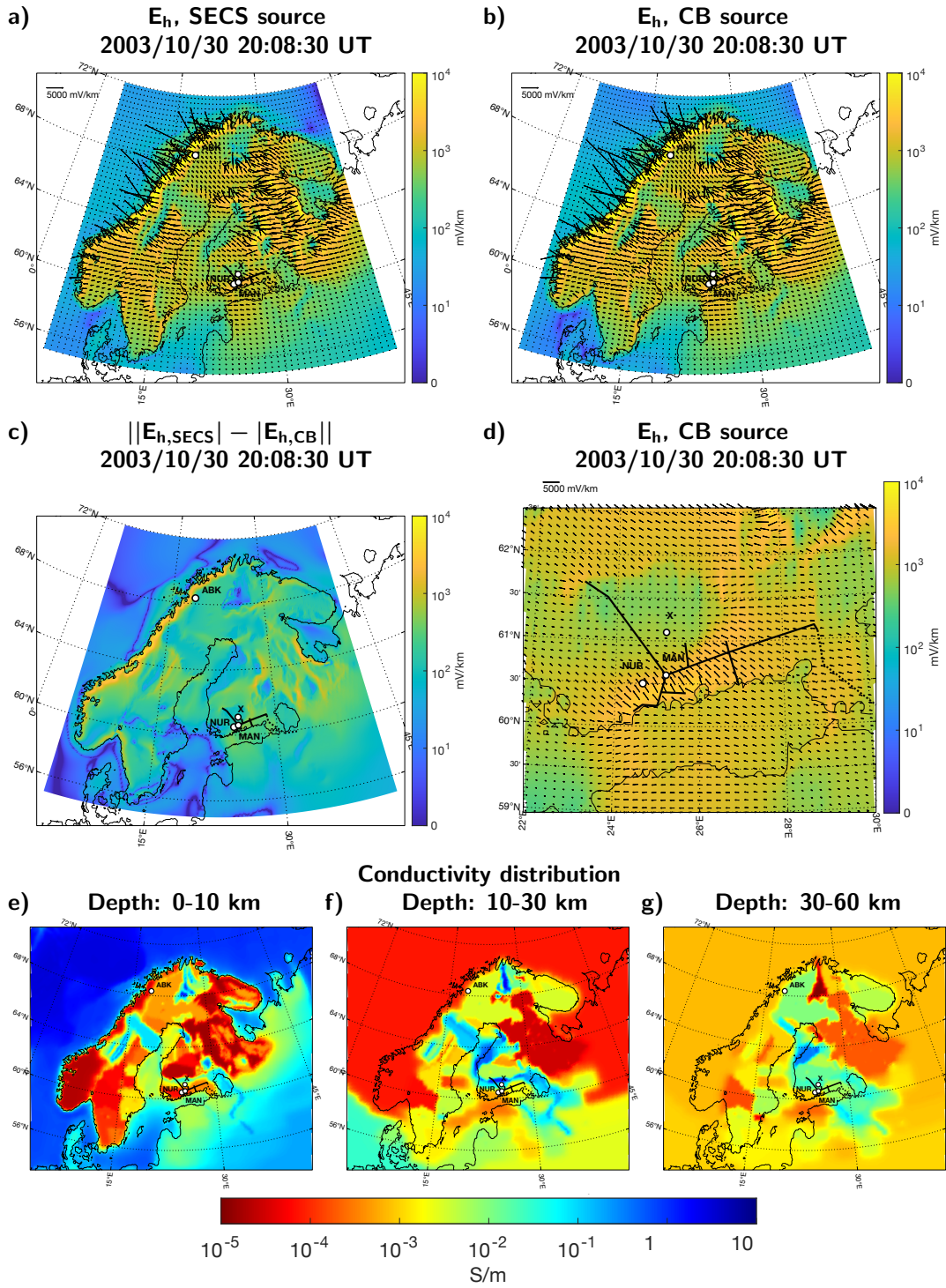


Figure 3. (a-b) Snapshots of the magnitude and direction of the GEF in Fennoscandia modeled using SECS and CB equivalent currents, at 20:08:30 UT, 30 October 2003. (c) The absolute difference between magnitudes of the GEF demonstrated in (a) and (b). (d) The magnitude and direction of the GEF in the area of the Finnish natural gas pipeline modeled with the use of the CB source at 20:08:30 UT, 30 October 2003. (e-g) Conductivity distribution in three layers of the 3-D part of the conductivity model. Finnish natural gas pipeline network is marked in all figures. IMAGE sites Abisko (ABK) and Nurmijärvi (NUR) as well as Mäntsälä (MAN) pipeline GIC recording site and Point X located 0.5° north of MAN are marked with white circles.

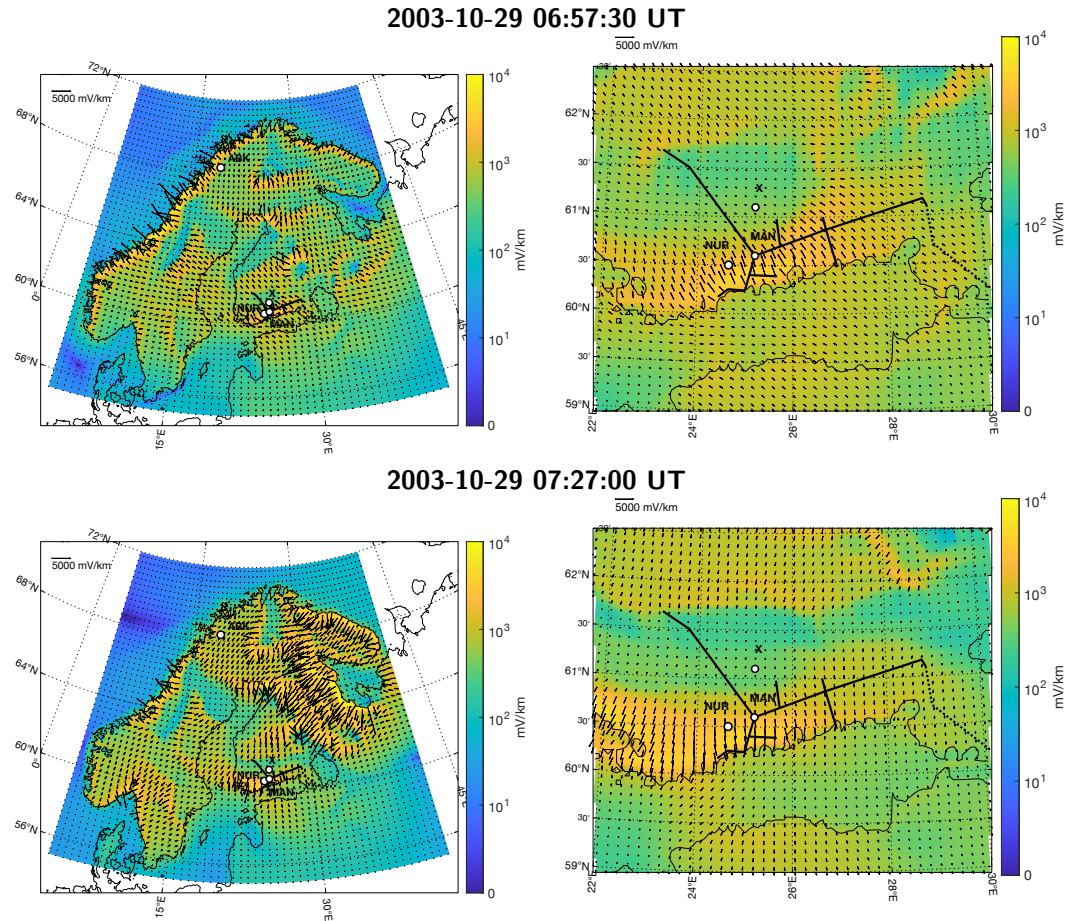


Figure 4. Snapshots of the magnitude and direction of the GEF across Fennoscandia (left) and in the Finnish natural gas pipeline area (right) modeled using the CB source at 06:57:30 UT, 29 October 2003 (top), and 07:27:00 UT, 29 October 2003 (bottom). Finnish natural gas pipeline network is marked in all figures. IMAGE sites Abisko (ABK) and Nurmijärvi (NUR) as well as Mäntsälä (MAN) pipeline GIC recording site and Point X located 0.5° north of MAN are marked with white circles.

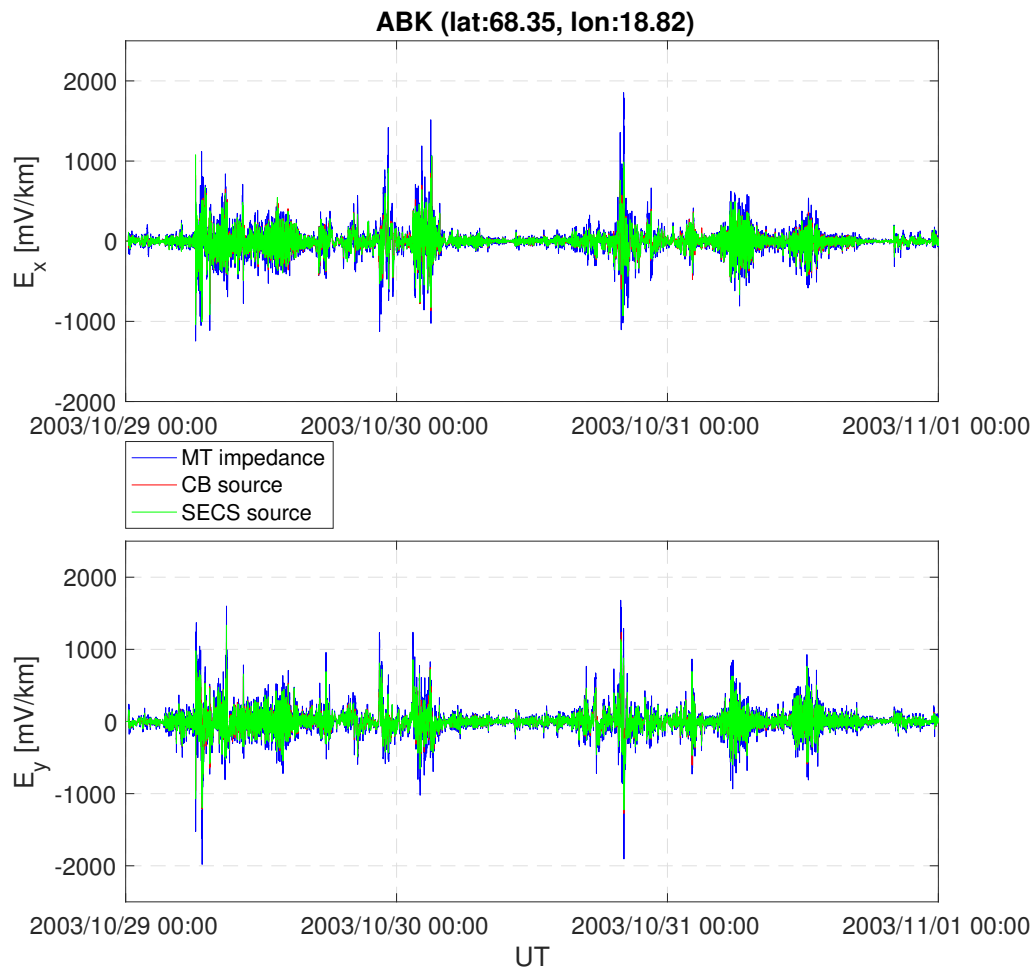


Figure 5. Time series of the GEF at the Abisko (ABK) geomagnetic observatory modeled using SECS, CB and MT approaches.

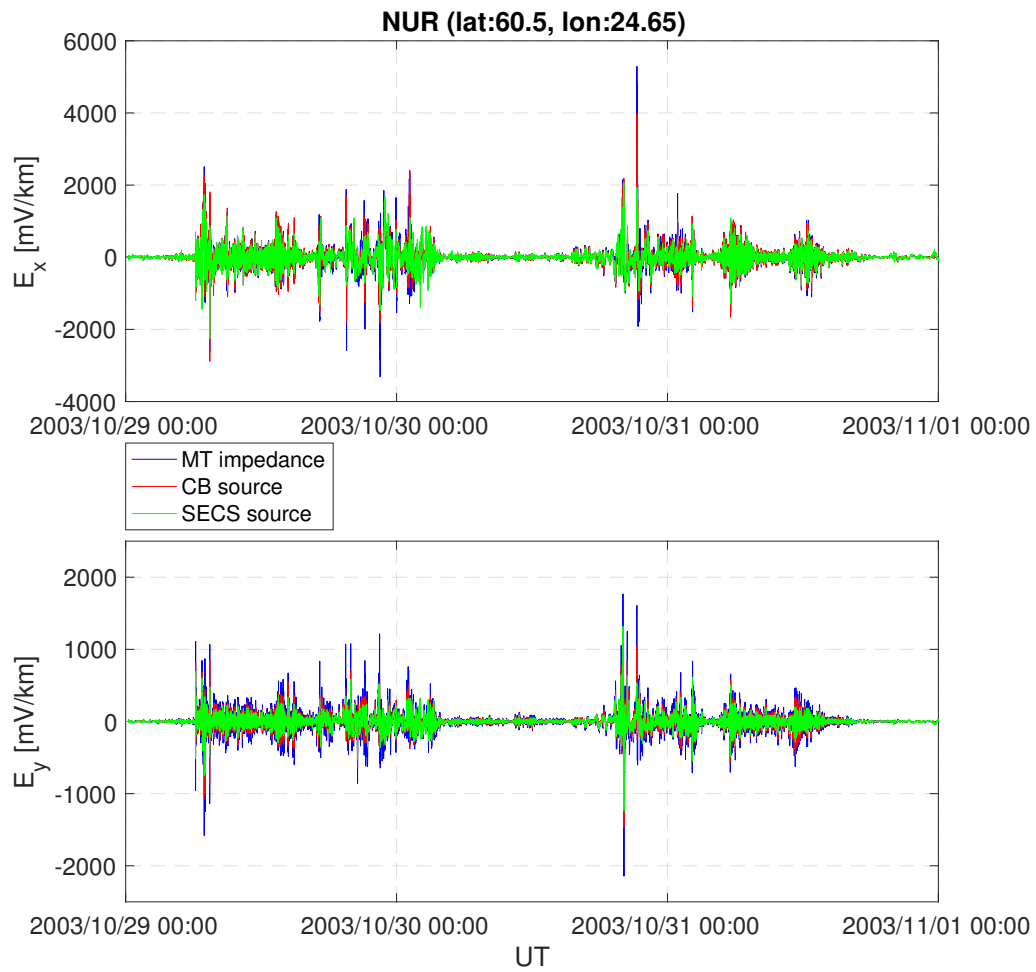


Figure 6. The same caption as in Figure 5 but for the Nurmijärvi (NUR) geomagnetic observatory.

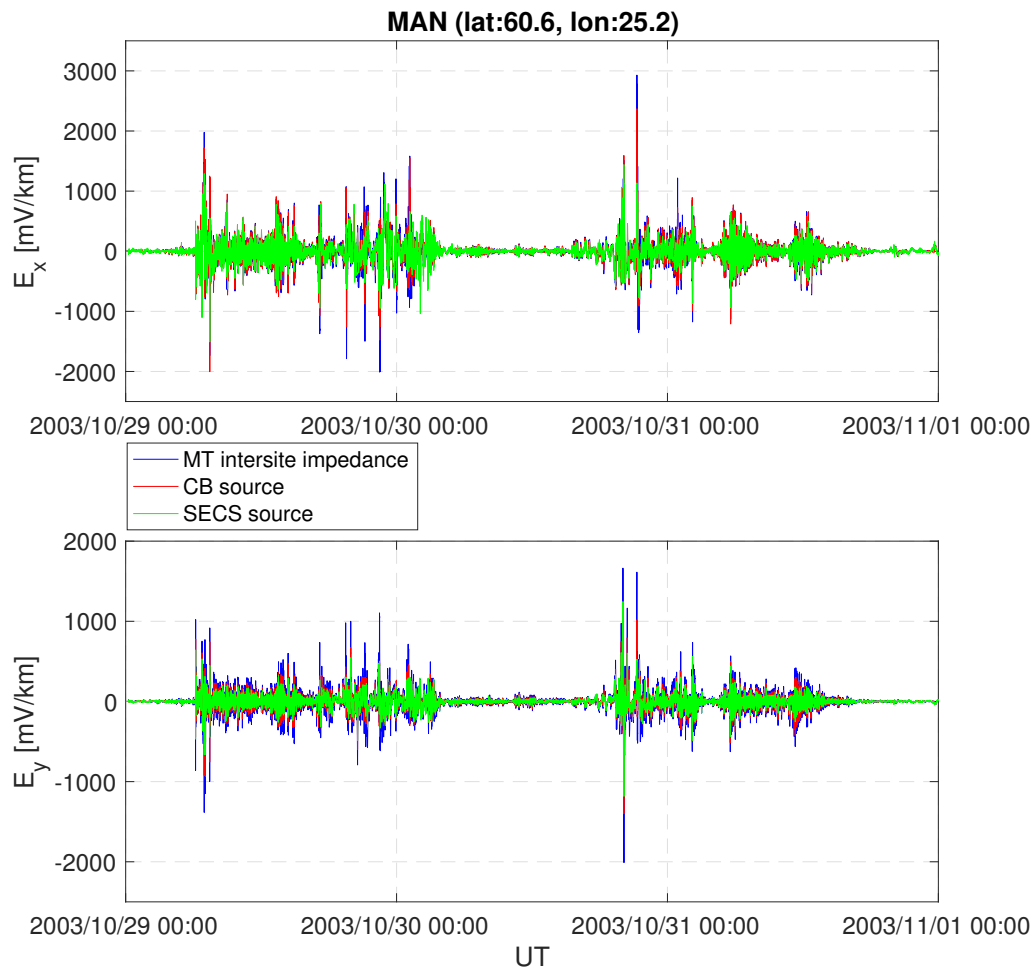


Figure 7. The same caption as in Figure 5 but for the Mäntsälä (MAN) natural gas pipeline GIC recording site.

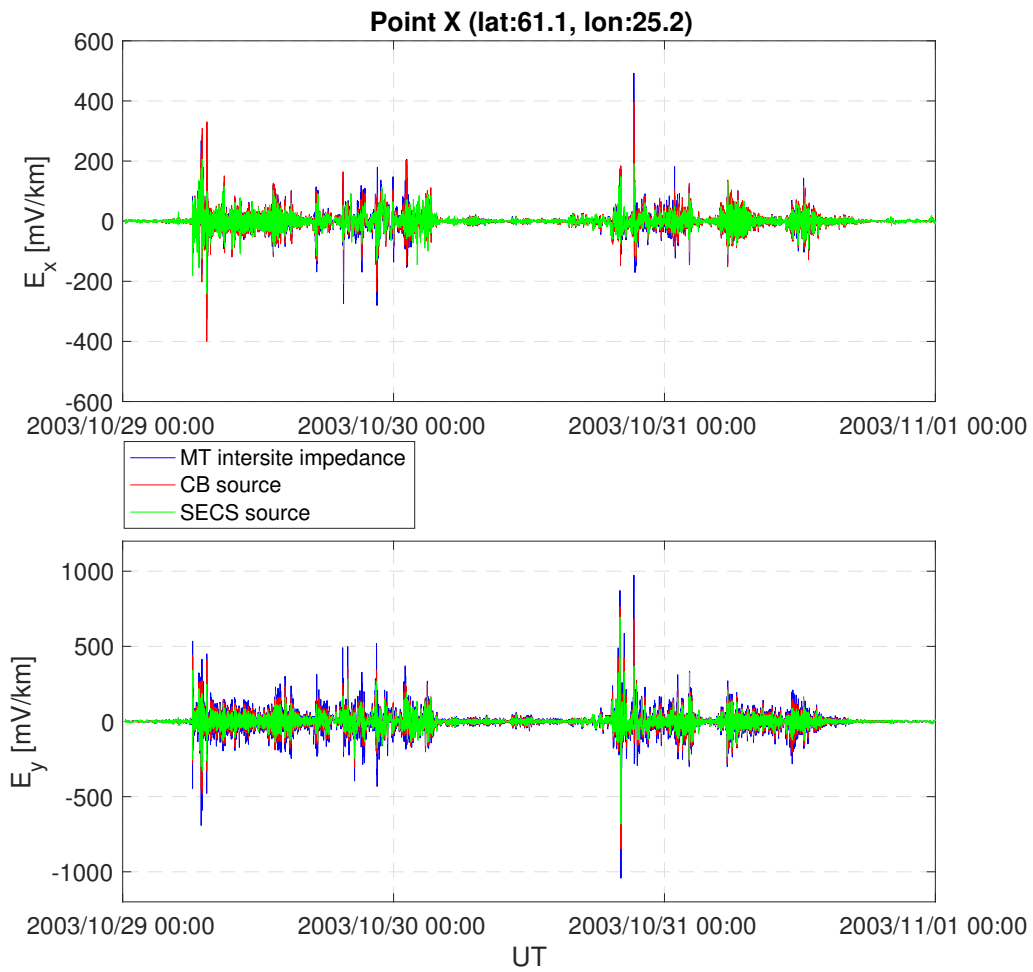


Figure 8. The same caption as in Figure 5 but for Point X located 0.5° north of Mäntsälä natural gas pipeline GIC recording site.

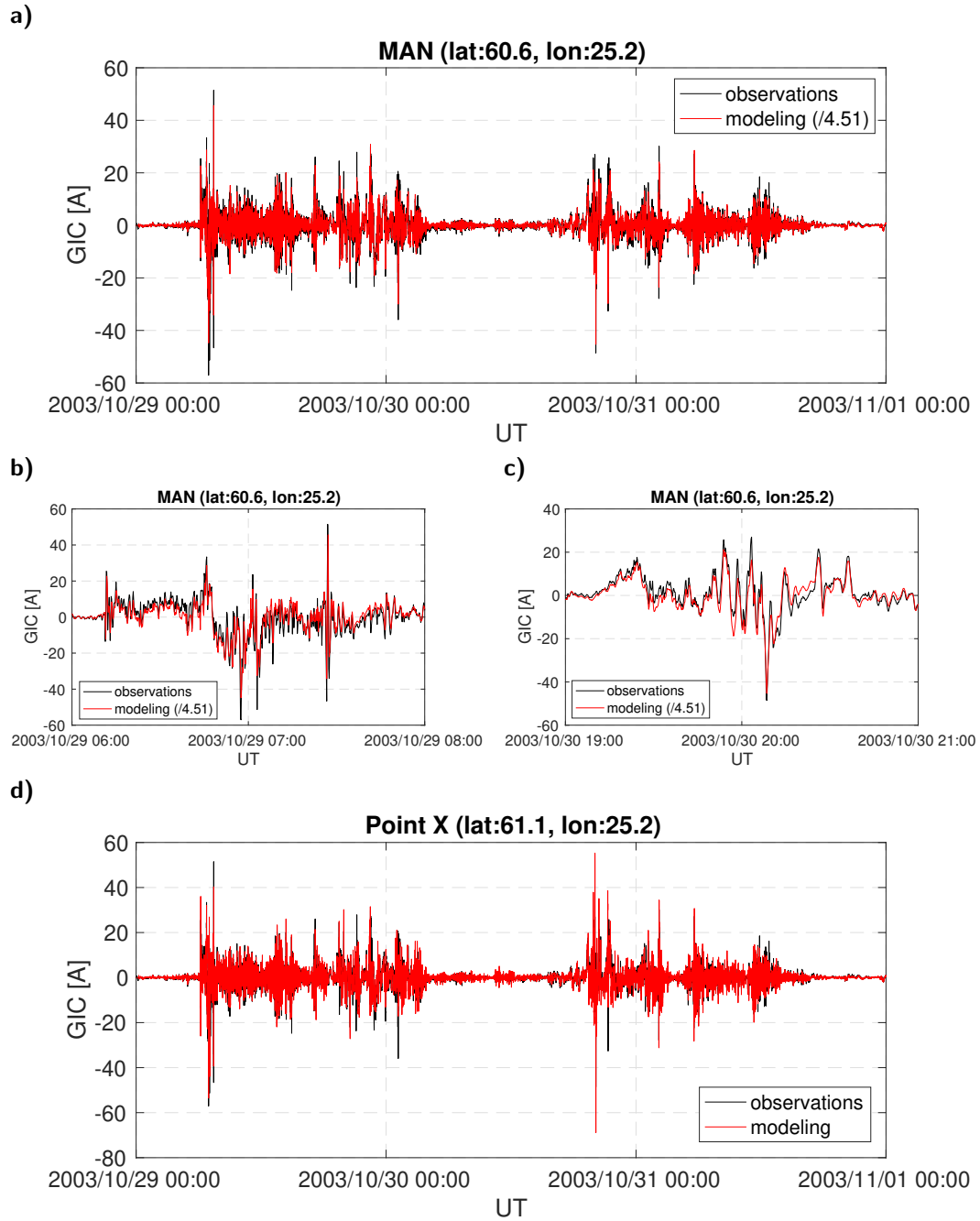


Figure 9. (a) Time series of observed GIC and GIC calculated at the Mäntsälä (MAN) natural gas pipeline recording point. (b-c) Time series of GIC observed and modeled at MAN at time intervals 06:00:00-08:00:00 UT, 29 October 2003, and 19:00:00-21:00:00 UT, 30 October 2003. (d) Time series of GIC observed and modeled at Point X located 0.5° north of MAN. Note that modeled GIC is scaled by a factor of 4.51 in Figures (a-c), while there is no scaling in Figure (d). GIC in all figures were calculated based on the GEF modeled using the CB source.